

## STATISTICAL PROPERTIES OF GAMMA-RAY BURST POLARIZATION

KENJI TOMA<sup>1,2</sup>, TAKANORI SAKAMOTO<sup>3,4</sup>, BING ZHANG<sup>5</sup>, JOANNE E. HILL<sup>3,6</sup>, MARK L. MCCONNELL<sup>7</sup>, PETER F. BLOSER<sup>7</sup>,  
RYO YAMAZAKI<sup>8</sup>, KUNIHITO IOKA<sup>9</sup>, AND TAKASHI NAKAMURA<sup>10</sup>

<sup>1</sup> Department of Astronomy and Astrophysics, Pennsylvania State University, 525 Davey Lab, University Park, PA 16802, USA; [toma@astro.psu.edu](mailto:toma@astro.psu.edu)

<sup>2</sup> Division of Theoretical Astronomy, National Astronomical Observatory of Japan, 2-21-1 Osawa, Mitaka, Tokyo 181-8588, Japan

<sup>3</sup> CRESST and NASA Goddard Space Flight Center, Greenbelt, MD 20771, USA

<sup>4</sup> Joint Center for Astrophysics, University of Maryland, Baltimore County, 1000 Hilltop Circle, Baltimore, MD 21250, USA

<sup>5</sup> Department of Physics and Astronomy, University of Nevada Las Vegas, Las Vegas, NV 89154, USA

<sup>6</sup> Universities Space Research Association, 10211 Wincopin Circle, Suite 500, Columbia, MD, 21044-3432, USA

<sup>7</sup> Space Science Center, University of New Hampshire, Durham, NH 03824, USA

<sup>8</sup> Department of Physical Science, Hiroshima University, Higashi-Hiroshima, Hiroshima 739-8526, Japan

<sup>9</sup> Theory Division, KEK (High Energy Accelerator Research Organization), 1-1 Oho, Tsukuba 305-0801, Japan

<sup>10</sup> Department of Physics, Kyoto University, Kyoto 606-8502, Japan

Received 2008 December 12; accepted 2009 April 6; published 2009 May 27

### ABSTRACT

The emission mechanism and the origin and structure of magnetic fields in gamma-ray burst (GRB) jets are among the most important open questions concerning the nature of the central engine of GRBs. In spite of extensive observational efforts, these questions remain to be answered and are difficult or even impossible to infer with the spectral and light-curve information currently collected. Polarization measurements will lead to unambiguous answers to several of these questions. Recent developments in X-ray and  $\gamma$ -ray polarimetry techniques have demonstrated a significant increase in sensitivity, enabling several new mission concepts, e.g., *Polarimeters for Energetic Transients (POET)*, providing wide field of view and broadband polarimetry measurements. If launched, missions of this kind would finally provide definitive measurements of GRB polarizations. We perform Monte Carlo simulations to derive the distribution of GRB polarizations in three emission models; the synchrotron model with a globally ordered magnetic field (SO model), the synchrotron model with a small-scale random magnetic field (SR model), and the Compton drag model (CD model). The results show that *POET*, or other polarimeters with similar capabilities, can constrain the GRB emission models by using the statistical properties of GRB polarizations. In particular, the ratio of the number of GRBs for which the polarization degrees can be measured to the number of GRBs that are detected ( $N_m/N_d$ ) and the distributions of the polarization degrees ( $\Pi$ ) can be used as the criteria. If  $N_m/N_d > 30\%$  and  $\Pi$  is clustered between 0.2 and 0.7, the SO model will be favored. If, instead,  $N_m/N_d < 15\%$ , then the SR or CD model will be favored. If several events with  $\Pi > 0.8$  are observed, then the CD model will be favored.

*Key words:* gamma rays: bursts – magnetic fields – polarization – radiation mechanisms: non-thermal

*Online-only material:* color figures

### 1. INTRODUCTION

Gamma-ray bursts (GRBs) are brief, intense flashes of  $\gamma$ -rays originating at cosmological distances, and they are the most luminous objects in the universe. They also have broadband afterglows long-lasting after the  $\gamma$ -ray radiation has ceased. It has been established that the bursts and afterglows are emitted from outflows moving toward us at highly relativistic speeds (Taylor et al. 2004), and at least some GRBs are associated with the collapse of massive stars (e.g., Hjorth et al. 2003; Stanek et al. 2003). Observations suggest that the burst is produced by internal dissipation within the relativistic jet that is launched from the center of the explosion, and the afterglow is the synchrotron emission of electrons accelerated in a collisionless shock driven by the interaction of the jet with the surrounding medium (for recent reviews, see Piran 2005; Mészáros 2006; Zhang 2007).

In spite of extensive observational and theoretical efforts, several key questions concerning the nature of the central engines of the relativistic jets and the jets themselves remain poorly understood. In fact, some of these questions are very difficult or even impossible to answer with the spectral and light-curve information currently collected. On the other hand, polarization

information, if retrieved, would lead to unambiguous answers to these questions. In particular, polarimetric observations of GRBs can address the following.

1. *Magnetic composition of GRB jets.* It is highly speculated that strong magnetic fields are generated at the GRB central engine and may play an essential role in the launch of the relativistic jets. However, it is unclear whether the burst emission region is penetrated by a globally structured, dynamically important magnetic field, and whether the burst is due to shock dissipation or magnetic reconnection (e.g., Spruit et al. 2001; Zhang & Mészáros 2002; Lyutikov et al. 2003).
2. *Emission mechanisms of the bursts.* The leading model for the emission mechanism of the prompt burst emission is synchrotron emission from relativistic electrons in a globally ordered magnetic field carried from the central engine, or random magnetic fields generated in situ in the shock dissipation region (Rees & Mészáros 1994). Other suggestions include Compton drag of ambient soft photons (Shaviv & Dar 1995; Eichler & Levinson 2003; Levinson & Eichler 2004; Lazzati et al. 2004), synchrotron self-Compton emission (Panaitescu & Meszaros 2000), and the combination of a thermal component from the photosphere

and a nonthermal component (e.g., synchrotron; Ryde et al. 2006; Thompson et al. 2007; Ioka et al. 2007).

3. *Geometric structure of GRB jets.* Although it is generally believed that GRB outflows are collimated, the distribution of the jet opening angles, the observer's viewing direction, and whether there are small-scale structures within the global jet are not well understood (Zhang et al. 2004; Yamazaki et al. 2004; Toma et al. 2005).

To date, robust positive detections of GRB polarization have been made only in the optical band in the afterglow phase. Varying linear polarizations have been observed in several optical afterglows several hours after the burst trigger, with a level of  $\sim 1\%$ – $3\%$ , which is consistent with the synchrotron emission mechanism of GRB afterglow (for reviews, see Covino et al. 2004; Lazzati 2006). An upper limit ( $< 8\%$ ) has been obtained for the early ( $t \sim 200$  s) optical afterglow of GRB 060418 (Mundell et al. 2007). Also, for radio afterglows, we have several upper limits for the polarization degree (Taylor et al. 2005; Granot & Taylor 2005) (for some implications, see Toma et al. 2008). As for the prompt burst emission, the strong linear polarization of the  $\gamma$ -ray emission at a level of  $\Pi = 80 \pm 20\%$  was claimed for GRB 021206 based on an analysis of *RHESSI* data (Coburn & Boggs 2003), although this claim remains controversial because of large systematic uncertainties (Rutledge & Fox 2004; Wigger et al. 2004). Several other reports of high levels of polarization in the prompt burst emission are also statistically inconclusive (Willis et al. 2005; Kalemci et al. 2007; McGlynn et al. 2007).

Recently, more sensitive observational techniques for X-ray and  $\gamma$ -ray polarimetry have been developed, and there are several polarimeter mission concepts. These include *Polarimeters for Energetic Transients (POET)* (Hill et al. 2008; Bloser et al. 2009), *Polarimeter of Gamma-ray Observer (PoGO)* (Mizuno et al. 2005), *POLAR* (Produit et al. 2005), *Advanced Compton Telescope (ACT)* (Boggs et al. 2006), *Gravity and Extreme Magnetism (GEMS)* (Jahoda et al. 2007), *XPOL* (Costa et al. 2007), *Gamma-ray Burst Investigation via Polarimetry and Spectroscopy (GRIPS)* (Greiner et al. 2008), and so on.

Several of these missions, if launched, would provide definitive detections of the burst polarizations and enable us to discuss the statistical properties of the polarization degrees and polarization spectra. Although there are several polarimetry mission concepts described in the literature, *POET* is the only one to date that incorporates a broadband capability for measuring the prompt emission from GRBs, and for this reason it provides a good case study for our simulations. *POET* will make measurements with two different polarimeters, both with wide fields of view (FoVs). The Gamma-Ray Polarimeter Experiment (GRAPE; 60–500 keV) and the Low Energy Polarimeter (LEP; 2–15 keV) provide a broad energy range for the observations. Suborbital versions of both *POET* instruments are currently being prepared for flight within the next few years. GRAPE will fly on a suborbital balloon in 2011, and the Gamma-Ray Burst Polarimeter (GRBP; a smaller version of LEP) will fly on a sounding rocket.

Theoretically, it has been shown that similarly high levels of linear polarization can be obtained in several GRB prompt emission models; the synchrotron model with a globally ordered magnetic field, the synchrotron model with a small-scale random magnetic field (Granot 2003; Lyutikov et al. 2003; Nakar et al. 2003), and the Compton drag model (Lazzati et al. 2004; Eichler & Levinson 2003; Levinson & Eichler 2004; Shaviv & Dar 1995). Thus, the detections of GRB prompt emission

polarization would support these three models. In this paper, we show that these models can be distinguished by their statistical properties of observed polarizations. We performed detailed calculations of the distribution of polarization degrees by including realistic spectra of GRB prompt emission and assuming realistic distributions of the physical parameters of GRB jets, and show that *POET*, or other polarimeters with similar capabilities, can constrain the GRB emission models. We use the limits of *POET* for GRB detection and polarization measurements as realistic and fiducial limits.

This paper is organized as follows. We first introduce the *POET* mission concept in Section 2. In Section 3, we summarize the properties of the observed linear polarization from uniform jets within the three emission models. Based on these models, we perform Monte Carlo simulations of observed linear polarizations and show how the statistical properties of observed polarization may constrain GRB emission mechanisms in Section 4. The summary and discussion are given in Section 5.

## 2. PROPERTIES OF POET SATELLITE

*POET* is a Small Explorer (SMEX) mission concept that will provide highly sensitive polarimetric observations of GRBs and can also make polarimetry measurements of solar flares, pulsars, soft gamma-ray repeaters, and slow transients. The payload consists of two wide FoV instruments: an LEP capable of polarization measurements in the 2–15 keV energy range and a high energy polarimeter (GRAPE) that will measure polarization in the 60–500 keV energy range. *POET* can measure GRB spectra from 2 keV up to 1 MeV. The *POET* spacecraft provides a zenith-pointed platform for maximizing the exposure to deep space and spacecraft rotation provides a means of effectively dealing with systematics in the polarization response. *POET* provides sufficient sensitivity and sky coverage to detect up to 200 GRBs in a two-year mission.

LEP and GRAPE determine polarization by measuring the number of events versus the event azimuth angle (EAA) as projected onto the sky. This is referred to as a modulation profile and represents a measure of the polarization magnitude and direction of polarization for the incident beam. Depending on the type of polarimeter, the EAA is either the direction of the ejected photoelectron (LEP) or the direction of the scattered photon (GRAPE). The response of a polarimeter to 100% polarized photons can be quantified in terms of the modulation factor,  $\mu$ , which is given by

$$\mu = \frac{C_{\max} - C_{\min}}{C_{\max} + C_{\min}}, \quad (1)$$

where  $C_{\max}$  and  $C_{\min}$  are the maximum and minimum of the modulation profile, respectively. The polarization fraction ( $\Pi$ ) of the incident flux is obtained by dividing the measured modulation by that expected for 100% polarized flux. The polarization angle ( $\Phi_0$ ) corresponds either to the maximum of the modulation profile (LEP) or to the minimum of the modulation profile (GRAPE). To extract these parameters from the data, the modulation histograms are fit to the functional form

$$C(\Phi) = A + B \cos^2(\Phi - \Phi_0). \quad (2)$$

The sensitivity of a polarimeter is defined in terms of the minimum detectable polarization (MDP), which refers to the minimum level of polarization that is detectable with a given observation (or, equivalently, the apparent polarization arising

**Table 1**  
Instrument Parameters

	GRAPE	LEP
Polarimetry	60–500 keV	2–15 keV
Detectors	BGO/plastic scintillator (62)	Ne:CO <sub>2</sub> :CH <sub>3</sub> NO <sub>2</sub> Gas (8)
Spectroscopy	15 keV–1 MeV	2–15 keV
Detectors	NaI(Tl) scintillator (2)	Ne:CO <sub>2</sub> :CH <sub>3</sub> NO <sub>2</sub> Gas (8)
Field of view	±60°	±44°

from statistical fluctuations in unpolarized data). The precise value of the MDP will depend on the source parameters (fluence, spectrum, etc.) and the polarimeter characteristics. At the 99% confidence level, the MDP can be expressed as

$$\text{MDP} = \frac{4.29}{\mu R_s} \sqrt{\frac{R_s + R_b}{t}}, \quad (3)$$

where  $R_s$  is the observed source strength (cts s<sup>-1</sup>),  $R_b$  is the total observed background rate (cts s<sup>-1</sup>), and  $t$  is the observing time (s). The ultimate sensitivity, however, may not be limited by statistics but by systematic errors created by false modulations that arise from azimuthal asymmetries in the instrument.

At energies from ~50 keV up to several MeV, photon interactions are dominated by Compton scattering. The operational concept for GRAPE is based on the fact that, in Compton scattering, photons are preferentially scattered at a right angle to the incident electric field vector (the polarization vector; Blosler et al. 2009, 2006; Jason et al. 2005). If the incident beam of photons is polarized, the azimuthal distribution of scattered photons will be asymmetric. The direction of the polarization vector is defined by the minimum of the scatter angle distribution. The GRAPE performance characteristics are shown in Table 1. The design of the GRAPE instrument is very modular, with 62 independent polarimeter modules and 2 spectroscopy modules. Each polarimeter module incorporates an array of optically independent 5 × 5 × 50 mm<sup>3</sup> nonhygroscopic scintillator elements aligned with and optically coupled to the 8 × 8 scintillation light sensors of a 64 channel MAPMT. Two types of scintillators are employed. Low-Z plastic scintillator is used as an effective medium for Compton scattering. High-Z inorganic scintillator (Bismuth Germanate, BGO) is used as a calorimeter, for absorbing the full energy of the scattered photon. The arrangement of scintillator elements within a module has 28 BGO calorimeter elements surrounding 32 plastic scintillator scattering elements. Valid polarimeter events are those in which a photon Compton scatters in one of the plastic elements and is subsequently absorbed in one of the BGO elements. These events can be identified as a coincident detection between one plastic scintillator element and one BGO calorimeter element. The azimuthal scatter angle is determined for each valid event by the relative locations of hit scintillator elements. It is not necessary to know where within each element the interaction takes place (e.g., the depth of interaction). It is sufficient to know only the lateral location of each element to generate a histogram of photon scatter angles.

At energies below ~ 50 keV, the most sensitive technique for broadband polarimetry is the photoelectric effect. The LEP measures the polarization of incident photons with the innovative operation of a Time Projection Chamber (TPC; Black et al. 2007). The LEP polarimeter enclosure consists of four dual-readout detector modules, each with an isolated gas volume contained by a Be X-ray window. Each detector module contains two 6 × 12 × 24 cm<sup>3</sup> (LxWxH) TPCs that share a single X-ray

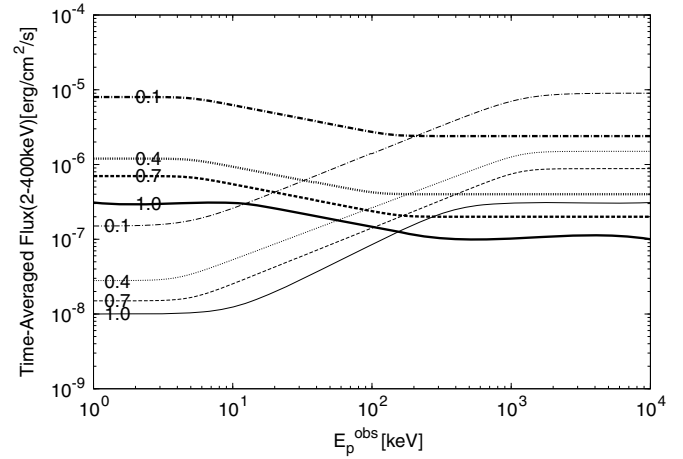


**Figure 1.** Contour of MDPs (i.e., the minimum values of polarization that is detectable at the 99% confidence level) of GRAPE (thick lines) and LEP (thin lines) for variable  $E_{p,obs}$  and  $F$  and for fixed  $\alpha = -0.2$ ,  $\beta = 1.2$ ,  $T = 20$  s and the incident angle  $30^\circ$ , where  $E_{p,obs}$  is the observed photon energy at the spectral peak,  $F$  is the time-averaged flux in 2–400 keV,  $\alpha$  and  $\beta$  are the lower and higher indices of the  $F_\nu$  spectrum, respectively, and  $T$  is the duration of the prompt emission. The combination of GRAPE and LEP enables us to measure polarizations with reasonable sensitivity in a very wide energy range.

transparent drift electrode. Each TPC comprises a micropattern proportional counter, consisting of a shared drift electrode and a high-field gas electron multiplier (GEM) positioned 1 mm from a strip readout plane. When an X-ray is absorbed in the gas between the drift electrode and the GEM, a photoelectron is ejected in a preferential direction with a  $\cos^2 \Phi$  distribution, where  $\Phi$  is the azimuthal angle measured from the X-ray polarization vector. As the photoelectron travels through the gas, it creates a path of ionization that drifts in a moderate, uniform field to the GEM where an avalanche occurs. The charge finally drifts to the strip detector where it is read out.

To estimate realistic MDP values for GRBs detected by GRAPE and LEP, we perform an analytical calculation for LEP and a Monte Carlo simulation for GRAPE using the current instrument configuration (Table 1). The input spectrum in the calculation and the simulation is a typical GRB spectrum which can be described as a smoothly broken power-law spectra characterized by photon energy at the  $\nu F_\nu$  spectral peak,  $E_{p,obs}$ , and lower and higher indices of the  $F_\nu$  spectrum,  $\alpha$  and  $\beta$ , respectively (Band et al. 1993). (We treat the spectral indices of the specific energy flux  $F_\nu$ , while Band et al. 1993 define  $\alpha_B$  and  $\beta_B$  as the indices of the photon number flux, i.e.,  $\alpha = -(\alpha_B + 1)$  and  $\beta = -(\beta_B + 1)$ , since we will calculate the net polarizations by using specific energy fluxes (Equation (7)).) The various  $E_{p,obs}$  and time-averaged flux in 2–400 keV,  $F$ , are investigated with fixed  $\alpha = -0.2$ ,  $\beta = 1.2$ , and a burst duration of  $T = 20$  s. We also assume the incident angle of bursts to be  $30^\circ$  off-axis. We interpret simulated events with  $\Pi > \text{MDP}$  as “ $\Pi$ -measurable events.” Figure 1 shows the contour of the MDP values in the  $E_{p,obs} - F$  plane for GRAPE and LEP. As can be seen in the figure, with the combination of LEP and GRAPE, it is possible to measure the polarization of GRBs with  $E_{p,obs}$  ranging from a few keV to MeV with reasonable sensitivity.

### 3. THEORETICAL MODELS

We calculate the linear polarization for instantaneous emission from a thin spherical shell moving radially outward with a bulk Lorentz factor  $\gamma \gg 1$  and an opening angle  $\theta_j$ .

The comoving frame emissivity has the functional form of  $j_{\nu'}^I = A_0 f(\nu') \delta(t' - t'_0) \delta(r' - r'_0)$ , where  $A_0$  is the normalization which may depend on direction in the comoving frame and other physical quantities of the shell and  $f(\nu')$  represents the spectral shape. A prime represents the physical quantities in the comoving frame. The delta functions describe the instantaneous emission at  $t = t_0$  and  $r = r_0$ . The normalization,  $A_0$ , has units of  $\text{erg cm}^{-2} \text{str}^{-1} \text{Hz}^{-1}$ . Using the spherical coordinate system  $(r, \theta, \phi)$  in the lab frame, where  $\theta = 0$  is the line of sight, we obtain the spectral fluence (Granot et al. 1999; Woods & Loeb 1999; Ioka & Nakamura 2001)

$$I_\nu = \frac{1+z}{d_L^2} \int d\phi \int d(\cos\theta) r_0^2 \frac{A_0 f(\nu')}{\gamma^2 (1 - \beta \cos\theta)^2}, \quad (4)$$

where  $z$  and  $d_L$  are the redshift and the luminosity distance of the source, respectively, and  $\nu' = (1+z)\nu\gamma(1 - \beta \cos\theta)$ . The integration is performed within the jet cone so that it depends on the viewing angle  $\theta_v$ , i.e., the angle between the jet axis and the line of sight. The corresponding Stokes parameters of the local emission (i.e., the emission from a given point on the shell) are given by  $j_{\nu'}^Q = j_{\nu'}^I \Pi_0' \cos(2\chi')$  and  $j_{\nu'}^U = j_{\nu'}^I \Pi_0' \sin(2\chi')$ , where  $\Pi_0'$  and  $\chi'$  are the polarization degree and position angle of the local emission measured in the comoving frame, respectively. The Stokes parameters of the emission from the whole shell can be obtained by integrating those of the local emission similar to the intensity  $I_\nu$ :

$$\begin{Bmatrix} Q_\nu \\ U_\nu \end{Bmatrix} = \frac{1+z}{d_L^2} \int d\phi \int d(\cos\theta) r_0^2 \frac{A_0 f(\nu')}{\gamma^2 (1 - \beta \cos\theta)^2} \Pi_0' \begin{Bmatrix} \cos(2\chi') \\ \sin(2\chi') \end{Bmatrix}. \quad (5)$$

The polarization degree is Lorentz invariant, i.e.,  $\Pi_0' = \Pi_0$ . The position angle  $\chi$  is calculated by taking account of the Lorentz transformation of the electromagnetic waves, and it is measured from a fixed direction, which we choose to be the direction from the line of sight to the jet axis. Then, by calculating  $\{I, Q, U\} = \int_{\nu_1}^{\nu_2} d\nu \{I_\nu, Q_\nu, U_\nu\}$ , we obtain the time-averaged linear polarization in the given wavebands  $[\nu_1, \nu_2]$ :

$$\Pi = \frac{\sqrt{Q^2 + U^2}}{I}. \quad (6)$$

We consider synchrotron and Compton drag (CD) mechanisms for the GRB prompt emission. In the synchrotron case, the magnetic field consists of a globally ordered field,  $\mathbf{B}_{\text{ord}}$ , and small-scale random field,  $\mathbf{B}_{\text{rnd}}$ , i.e.,  $\mathbf{B} = \mathbf{B}_{\text{ord}} + \mathbf{B}_{\text{rnd}}$ . The field  $\mathbf{B}_{\text{ord}}$  may originate from the central engine, while  $\mathbf{B}_{\text{rnd}}$  may be produced in the emission region itself. Here, we consider two extreme cases; the synchrotron model with an ordered field (SO), in which  $B_{\text{ord}}^2 \gg \langle B_{\text{rnd}}^2 \rangle$ , and a synchrotron model with a random field (SR), in which  $B_{\text{ord}}^2 \ll \langle B_{\text{rnd}}^2 \rangle$ . For the SO model, in particular, we assume a toroidal magnetic field. In the following subsections, we describe  $A_0$ ,  $f(\nu')$ ,  $\Pi_0$ , and  $\chi$  as functions of  $(\theta, \phi)$  for each model and calculate the linear polarization for given parameters  $\gamma$ ,  $\theta_j$ ,  $\theta_v$ , and  $z$ .

### 3.1. SO Model: Synchrotron with Ordered Field

The prompt emission of GRBs could be explained by synchrotron emission from accelerated electrons that have a non-thermal energy spectra by some dissipation process within the

jet, e.g., internal shocks. Synchrotron emission from the relativistically moving shell within a globally ordered magnetic field results in a net observed linear polarization, reflecting the direction of the field (Lyutikov et al. 2003; Granot 2003; Nakar et al. 2003). Let us assume that the jet is permeated by a toroidal field. This is a likely configuration if a magnetic field is advected by the jet with a constant speed from the central engine (e.g., Spruit et al. 2001; Fendt & Ouyed 2004).

A general formula for calculating the observed linear polarization for synchrotron emission from a uniform jet, in which the electrons have a single power-law energy spectrum and an isotropic pitch angle distribution and the magnetic field is ordered globally, is derived by Granot (2003) and Granot & Taylor (2005). Here, we adopt their formulation and extend it for the electrons having a broken power-law energy spectrum in order to reproduce the typical observed spectra of GRBs (Band et al. 1993). We adopt the following form for the radiation spectrum:  $f(\nu') = \tilde{f}(x)$ , where  $x = \nu'/\nu_0'$  and

$$\tilde{f}(x) = \begin{cases} x^{-\alpha} e^{-x}, & \text{for } x \leq \beta - \alpha, \\ x^{-\beta} (\beta - \alpha)^{\beta - \alpha} e^{\alpha - \beta}, & \text{for } x \geq \beta - \alpha. \end{cases} \quad (7)$$

where  $\nu_0'$ ,  $\alpha$ , and  $\beta$  are the break frequency and low-energy and high-energy spectral indices of the comoving spectrum, respectively.<sup>11</sup> If we assume that the energy spectrum of the electrons and the strength of the magnetic field are uniform in the emitting shell, then we may write  $A_0 = (\sin\theta_B')^{\alpha+1}$ , where  $\theta_B'$  is the angle between the direction of the emitted radiation and the local direction of the magnetic field (Rybicki & Lightman 1979). The local polarization degree is given by

$$\Pi_0 = \Pi_0^{\text{syn}} \equiv \begin{cases} (\alpha + 1)/(\alpha + \frac{5}{3}), & \text{for } x \leq \beta - \alpha, \\ (\beta + 1)/(\beta + \frac{5}{3}), & \text{for } x \geq \beta - \alpha. \end{cases} \quad (8)$$

For a globally ordered magnetic field, the Faraday depolarization effect may be strong within the emitting region (e.g., Toma et al. 2008; Matsumiya & Ioka 2003; Sagiv et al. 2004), but we neglect it here for simplicity. By using a new variable  $y \equiv (\gamma\theta)^2$ , we obtain (see the Appendix)

$$\sin\theta_B' = \left[ \left( \frac{1-y}{1+y} \right)^2 + \frac{4y}{(1+y)^2} \frac{(a - \cos\phi)^2}{1+a^2 - 2a\cos\phi} \right]^{1/2}, \quad (9)$$

$$\chi = \phi + \arctan \left( \frac{1-y}{1+y} \frac{\sin\phi}{a - \cos\phi} \right), \quad (10)$$

where  $a = \theta/\theta_v$ . Then the formulation of the net polarization degree in the observed frequency region  $[\nu_1, \nu_2]$  becomes

$$\begin{aligned} \Pi &= \left| \int_{\nu_1}^{\nu_2} d\nu \int_0^{(1+q)^2 y_j} \frac{dy}{(1+y)^2} \right. \\ &\times \left. \int_{-\Delta\phi(y)}^{\Delta\phi(y)} d\phi \tilde{f}(x) (\sin\theta_B')^{\alpha+1} \Pi_0^{\text{syn}}(x) \cos(2\chi) \right| \\ &\times \left[ \int_{\nu_1}^{\nu_2} d\nu \int_0^{(1+q)^2 y_j} \frac{dy}{(1+y)^2} \int_{-\Delta\phi(y)}^{\Delta\phi(y)} d\phi \tilde{f}(x) (\sin\theta_B')^{\alpha+1} \right]^{-1}, \end{aligned} \quad (11)$$

<sup>11</sup> In our model, the radiation spectrum (Equation (7)) is thought to be produced by the broken power-law energy spectrum of electrons:  $N(\gamma_e) \propto \gamma_e^{-p_1}$  for  $\gamma_e < \gamma_0$  and  $N(\gamma_e) \propto \gamma_e^{-p_2}$  for  $\gamma_e > \gamma_0$ , where  $\alpha = (p_1 - 1)/2$  and  $\beta = (p_2 - 1)/2$ . This formulation also includes the case of  $p_1 < 1/3$ , in which  $\alpha = -1/3$ ,  $A_0 \propto (\sin\theta_B')^{2/3}$ , and  $\Pi_0^{\text{syn}} = 1/2$  for  $x \leq \beta - \alpha$  (Granot 2003).

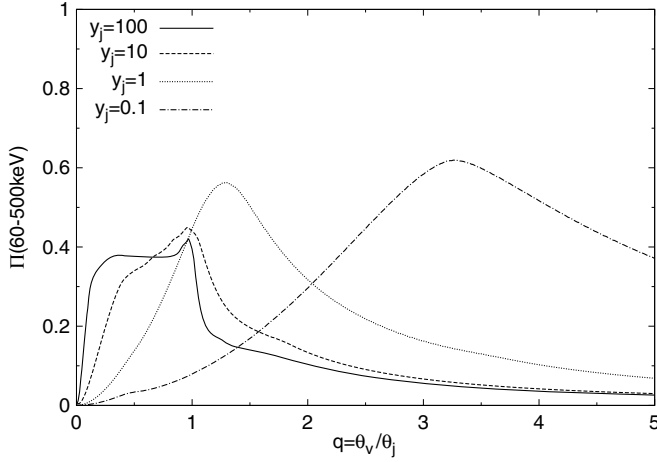


**Figure 2.** Linear polarization degrees in the 60–500 keV band as a function of  $q = \theta_v/\theta_j$ , where  $\theta_v$  is the viewing angle of the observer and  $\theta_j$  is the jet opening angle, for several values of  $y_j = (\gamma\theta_j)^2$ , calculated in the SO model (synchrotron model with globally ordered magnetic field). The other parameters are  $\gamma v'_0 = 350$  keV,  $\alpha = -0.2$ ,  $\beta = 1.2$ , and  $z = 1$ .

where  $x = (1+z)v(1+y)/2\gamma v'_0$ , and

$$q = \frac{\theta_v}{\theta_j}, \quad y_j = (\gamma\theta_j)^2, \quad (12)$$

$$\Delta\phi(y) = \begin{cases} 0, & \text{for } q > 1 \text{ and } y < (1-q)^2 y_j, \\ \pi, & \text{for } q < 1 \text{ and } y < (1-q)^2 y_j, \\ \cos^{-1} \left[ \frac{(q^2-1)y_j+y}{2q\sqrt{y_j y}} \right], & \text{otherwise.} \end{cases} \quad (13)$$

The polarization degree,  $\Pi$ , in the waveband  $[\nu_1, \nu_2]$  can be calculated if the geometrical parameters,  $y_j, q$ , the spectral parameters,  $\gamma v'_0, \alpha, \beta$ , and the redshift,  $z$ , are given.

Figure 2 shows the polarization degree in the 60–500 keV band as a function of  $q$  for several values of  $y_j$ . The other parameters are  $\gamma v'_0 = 350$  keV,  $\alpha = -0.2$ ,  $\beta = 1.2$ , and  $z = 1$ . The polarization degree is negligible for  $q \approx 0$ , because in this case the local polarization vectors are axisymmetric around the line of sight, i.e.,  $\chi = \phi$  (see the Appendix), and the local polarizations are canceled out. For  $y_j > 1$ , a high level of polarization is obtained for  $y_j^{-1/2} < q < 1$  (i.e.,  $\gamma^{-1} < \theta_v < \theta_j$ ). In this case, only a fraction of the emitting shell (i.e.,  $\theta < \gamma^{-1}$ ) is bright because of the relativistic beaming effect, and the direction of the magnetic field is quite ordered in the bright region. The contribution of the emission from high latitude,  $\theta > \gamma^{-1}$ , is negligible, especially for  $y_j \geq 100$ , so that the net polarization degree is determined only by the emission from the bright region with  $\theta < \gamma^{-1}$  and then it is nearly constant. The results of our calculations for the case of  $\alpha = \beta$  and  $y_j \geq 100$  are consistent with the results of Granot (2003) and Lyutikov et al. (2003). For  $y_j < 1$ , a high level of polarization is obtained for  $q \sim 1 + y_j^{-1/2}$  (i.e.,  $\theta_v \sim \theta_j + \gamma^{-1}$ ). In this case, the bright region on the emitting shell is small, also.

The polarization is higher for softer spectra (i.e., larger  $\alpha$  and  $\beta$ ). For example, for  $y_j = 100$ ,  $\gamma v'_0 = 350$  keV, and  $z = 1$ , the polarization degree at the plateau for  $q < 1$  is  $\simeq 0.28$  for  $\alpha = -0.5$  and  $\beta = 0.9$ , while it is  $\simeq 0.52$  for  $\alpha = 0.4$  and  $\beta = 1.8$ . This is caused mainly by the dependence of the synchrotron polarization on the spectral indices (Equation (8)). The maximum polarization degree obtained in the SO model is  $\simeq 0.8$  for  $y_j \geq 0.01$ ,  $\alpha \leq 0.4$ , and  $\beta \leq 1.8$ .

### 3.2. SR Model: Synchrotron with Random Field

If the magnetic field is produced at the shock itself within the jet, the directions of the field would be random on a scale as small as the plasma skin depth (Gruzinov & Waxman 1999; Medvedev & Loeb 1999). It is quite plausible that the directions of the field are not completely random, but have symmetry around the direction normal to the shock. The less isotropic the magnetic field directions behind the shock, the higher the local polarization. We consider the extreme case in which the field is random strictly within the plane of the shock. In this model, the directions of the local polarization vectors on the shell are axisymmetric around the line of sight (see below), so that no net polarization remains if the visible region,  $\theta < \gamma^{-1}$ , is wholly within the jet cone. However, if the observer views the jet from an off-axis angle and the symmetry is broken, a high level of polarization remains (Waxman 2003; Sari 1999; Ghisellini & Lazzati 1999).

Similar to the SO model, we adopt the broken power-law form of the spectrum:  $f(v') = \tilde{f}(x)$ , where  $x = v'/v'_0$  and  $\tilde{f}(x)$  is given by Equation (7). We assume that the energy distribution of the electrons and the strength of the magnetic field are uniform in the emitting shell. The local Stokes parameters are given by averaging them with respect to the magnetic field directions within the shock plane (see the Appendix). Thus, we may write  $A_0 = \langle (\sin \theta'_B)^{\alpha+1} \rangle$ , where  $\langle \rangle$  represents the average. The local polarization degree is given by  $\Pi_0 = \Pi_0^{\text{syn}} \langle (\sin \theta'_B)^{\alpha+1} \cos(2\phi'_B) \rangle / \langle (\sin \theta'_B)^{\alpha+1} \rangle$ , where

$$\langle (\sin \theta'_B)^{\alpha+1} \rangle = \frac{1}{\pi} \int_0^\pi d\eta' \left[ 1 - \frac{4y}{(1+y)^2} \cos^2 \eta' \right]^{(\alpha+1)/2}, \quad (14)$$

$$\langle (\sin \theta'_B)^{\alpha+1} \cos(2\phi'_B) \rangle = \frac{1}{\pi} \int_0^\pi d\eta' \left\{ \left[ 1 - \frac{4y}{(1+y)^2} \cos^2 \eta' \right]^{(\alpha-1)/2} \times \left[ \sin^2 \eta' - \left( \frac{1-y}{1+y} \right)^2 \cos^2 \eta' \right] \right\}. \quad (15)$$

The local polarization position angle measured in the lab frame is given by  $\chi = \phi$ ; therefore, we obtain the formulation for the net polarization in the observed frequency region  $[\nu_1, \nu_2]$ :

$$\Pi = \left| \int_{\nu_1}^{\nu_2} d\nu \int_0^{(1+q)^2 y_j} \frac{dy}{(1+y)^2} \tilde{f}(x) \Pi_0^{\text{syn}}(x) \times \langle (\sin \theta'_B)^{\alpha+1} \cos(2\phi'_B) \rangle \sin(2\Delta\phi(y)) \right| \times \left[ \int_{\nu_1}^{\nu_2} d\nu \int_0^{(1+q)^2 y_j} \frac{dy}{(1+y)^2} \tilde{f}(x) \langle (\sin \theta'_B)^{\alpha+1} \rangle 2\Delta\phi(y) \right]^{-1}, \quad (16)$$

where  $q = \theta_v/\theta_j$ ,  $y_j = (\gamma\theta_j)^2$ ,  $x = (1+z)v(1+y)/2\gamma v'_0$ , and  $\Pi_0^{\text{syn}}$  and  $\Delta\phi(y)$  are given by Equations (8) and (13), respectively.

Figure 3 shows the polarization degree in the 60–500 keV band as a function of  $q$  for several values of  $y_j$ . The other parameters are  $\gamma v'_0 = 350$  keV,  $\alpha = -0.2$ ,  $\beta = 1.2$ , and  $z = 1$ . The results of our calculations for the case of  $\alpha = \beta$  are consistent with those of Granot (2003) and Nakar et al. (2003). A high level of polarization is obtained for  $q \sim 1 + y_j^{-1/2}$  (i.e.,  $\theta_v \sim \theta_j + \gamma^{-1}$ ) for each value of  $y_j$ . Since the local polarization vectors are axisymmetric around the line of sight, the local polarizations are canceled out if the line of sight is within the jet cone. If the jet is observed from an off-axis angle, the net polarization remains. The local polarization degree is highest for emission where  $\theta = \gamma^{-1}$ , so that the net polarization has a maximum value. The

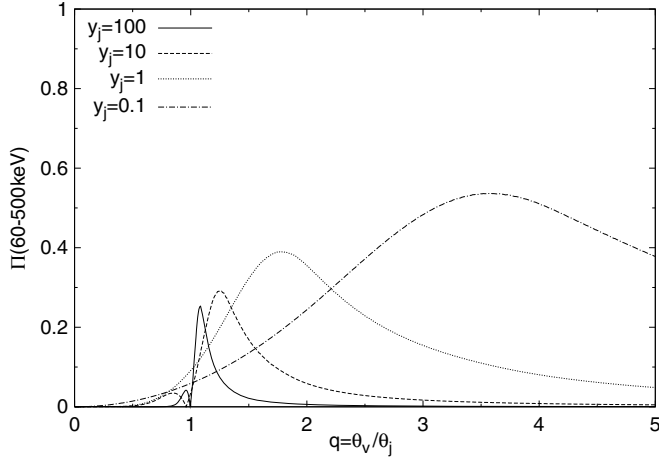


**Figure 3.** Same as Figure 2, but in the SR model (synchrotron model with small-scale random magnetic field).

maximum  $\Pi$  is higher for smaller  $y_j$ , because the contribution of the emission from high latitude points ( $\theta > \gamma^{-1}$ ), with a low level of local polarization, is smaller.

Similar to the SO model, the polarization is higher for softer spectra, mainly because of the dependence of the local polarization degree on frequency (Equation (8)). For example, for  $y_j = 1$ ,  $\gamma v'_0 = 350$  keV, and  $z = 1$ , the maximum polarization is  $\simeq 0.32$  for  $\alpha = -0.5$  and  $\beta = 0.9$ , while it is  $\simeq 0.49$  for  $\alpha = 0.4$  and  $\beta = 1.8$ . For  $y_j \geq 0.01$ ,  $\alpha \leq 0.4$ , and  $\beta \leq 1.8$ , the maximum polarization degree in the SR model is  $\simeq 0.8$ .

### 3.3. CD Model: Compton Drag Model

The prompt emission from GRBs could be produced by bulk inverse Comptonization of soft photons from the relativistic jet (Lazzati et al. 2004; Eichler & Levinson 2003; Levinson & Eichler 2004; Shaviv & Dar 1995). The local polarization position angles are symmetric around the line of sight, similar to the SR model. Therefore, this model also requires an off-axis observation of the jet to achieve a high level of polarization. However, the CD model is different from the SR model in the fact that the CD model can, in principle, achieve  $\Pi \sim 1$  under the most optimistic geometric configurations, whereas the maximum  $\Pi$  is  $\sim (\beta + 1)/(\beta + \frac{5}{3}) \sim 0.8$  in the SR model.

We assume that the seed radiation is unpolarized and has a nonthermal, isotropic spectrum, and the scattered radiation has the broken power-law spectrum  $f(v') = \tilde{f}(x)$ , where  $x = v'/v'_0$  and  $\tilde{f}(x)$  is given by Equation (7). If the intensity of the seed radiation and the electron number density of the shell are assumed to be uniform, then we may write  $A_0 = (1 + \cos^2 \theta')/2$ , and  $\Pi_0 = (1 - \cos^2 \theta')/(1 + \cos^2 \theta')$  (Rybicki & Lightman 1979; Begelman & Sikora 1987). The polarization vectors in the comoving frame are perpendicular to both incident and scattering directions of photons, so that we obtain  $\chi = \phi + \pi/2$  in the lab frame. Therefore, we achieve the formulation for the net linear polarization in the observed frequency region  $[v_1, v_2]$ :

$$\Pi = \left| \int_{v_1}^{v_2} dv \int_0^{(1+q)^2 y_j} \frac{dy}{(1+y)^2} \tilde{f}(x) \frac{2y}{(1+y)^2} \sin(2\Delta\phi(y)) \right| \times \left[ \int_{v_1}^{v_2} dv \int_0^{(1+q)^2 y_j} \frac{dy}{(1+y)^2} \tilde{f}(x) \frac{1+y^2}{(1+y)^2} 2\Delta\phi(y) \right]^{-1}, \quad (17)$$

where  $q = \theta_v/\theta_j$ ,  $y_j = (\gamma\theta_j)^2$ ,  $x = (1+z)v(1+y)/2\gamma v'_0$ , and  $\Delta\phi(y)$  is given by Equation (13).

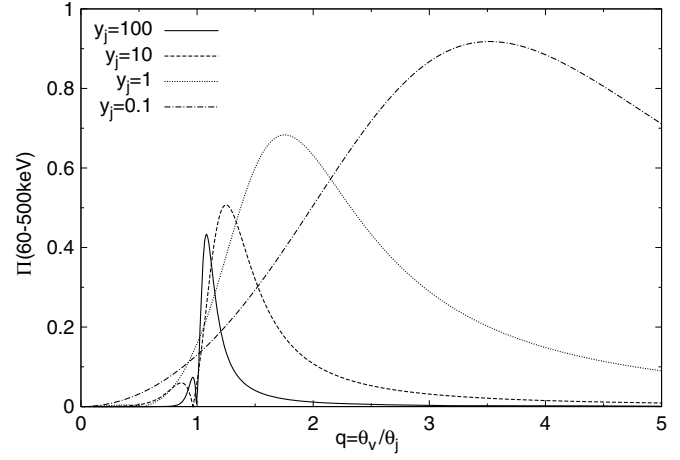


**Figure 4.** Same as Figure 2, but in the CD model (Compton drag model).

Figure 4 shows the polarization degree in the 60–500 keV band as a function of  $q$  for several values of  $y_j$ . The other parameters are  $\gamma v'_0 = 350$  keV,  $\alpha = -0.2$ ,  $\beta = 1.2$ , and  $z = 1$ . The results of our calculations for the case of  $\alpha = \beta$  are consistent with those of Lazzati et al. (2004). The results are similar to those of the SR model, but the polarization degree is higher than in the SR model.

The polarization is higher for softer spectra, although the local polarization degree is not dependent on the frequency in this model. For instance, for  $y_j = 1$ ,  $\gamma v'_0 = 350$  keV, and  $z = 1$ , the maximum polarization is  $\simeq 0.66$  for  $\alpha = -0.5$  and  $\beta = 0.9$ , while it is  $\simeq 0.71$  for  $\alpha = 0.4$  and  $\beta = 1.8$ , but the variation is smaller than for the synchrotron models (see Sections 3.1 and 3.2). This variation is caused by the kinematic effect. The local polarization degree is a maximum for  $\theta = \gamma^{-1}$  (i.e.,  $\theta' = \pi/2$ ). Thus, the net polarization is higher when the contribution of the emission from higher latitude with  $\theta > \gamma^{-1}$  is smaller. The high latitude emission is dimmer as the radiation spectrum is softer. Therefore, the net polarization is higher when the spectrum is softer. This effect also arises in the SO and SR models, although in those models the intrinsic dependence of polarization on the spectrum (Equation (8)) is rather strong (see Sections 3.1 and 3.2). For  $y_j \geq 0.01$ ,  $\alpha \leq 0.4$ , and  $\beta \leq 1.8$ , the maximum polarization degree for the CD model is  $\simeq 1.0$ .

## 4. STATISTICAL PROPERTIES

In this section, we show the results of our Monte Carlo simulation of the GRB prompt emission polarization. First, in Section 4.1, we give the values of the model parameters so that the observed fluences and peak energies of simulated bursts are consistent with the data obtained with the *HETE-2* satellite. In Section 4.2, we examine the properties of the polarization distribution of bursts detectable by the *POET* satellite, regardless of instrument MDP. Next, in Section 4.3, we show the distribution of polarizations that can be measured by *POET*, and discuss how we may constrain the emission models.

### 4.1. Model Parameters

We performed Monte Carlo simulations to obtain the distribution of the observed spectral energies and fluences in the three emission models. Such simulations have been developed to discuss the empirical correlation between spectral peak energies in the cosmological rest frame and isotropic  $\gamma$ -ray energies

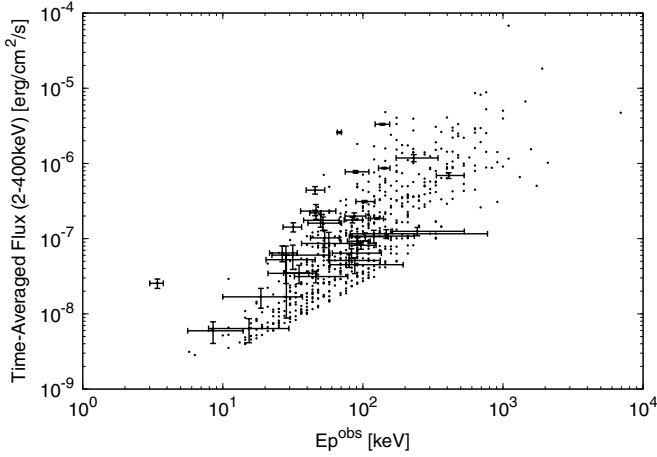


**Figure 5.**  $E_{p,\text{obs}} - F$  diagram calculated in our Monte Carlo simulation. The simulated events that can be detected by WXM on *HETE-2* are represented by dots. They are compared with the *HETE-2* data (points with errorbars; Sakamoto et al. 2005).

among GRBs and X-ray flashes in several models of geometrical structure of GRB jets (Zhang et al. 2004; Yamazaki et al. 2004; Dai & Zhang 2005; Toma et al. 2005; Donaghy 2006). We generated 10,000 GRB jets with Lorentz factor,  $\gamma$ , and opening angle,  $\theta_j$ , and a random viewing angle for each jet according to the probability distribution of  $\sin\theta_v d\theta_v d\phi$  with  $\theta_v < 0.22$  rad.<sup>12</sup> For each burst generated we calculate the  $\nu I_\nu$  spectrum to obtain the spectral peak energy,  $E_{p,\text{obs}}$ , and the fluence,  $I$ , in the 2–400 keV range by using Equation (4). Since  $E_{p,\text{obs}}$ 's and  $I$ s calculated for each  $q = \theta_v/\theta_j$  in the three models are different only by factors less than 2,  $E_{p,\text{obs}}$ 's and  $I$ s of the simulated bursts may be calculated using just one model, for which we chose the CD model.

The distributions of  $\gamma$  and  $\theta_j$  for GRB jets are highly uncertain. We make a simple assumption for the distribution and in Section 4.3 we perform some simulations for different assumptions. We fix  $\gamma = 100$ . We assume the distribution of  $\theta_j$  as

$$f(\theta_j)d\theta_j \propto \begin{cases} \theta_j^{q_1} d\theta_j, & \text{for } 0.001 \leq \theta_j \leq 0.02, \\ \theta_j^{q_2} d\theta_j, & \text{for } 0.02 \leq \theta_j \leq 0.2, \end{cases} \quad (18)$$

where  $q_1 = 0.5$  and  $q_2 = -2.0$ . The value of  $q_2 = -2$  is inferred from the observations of the steepening breaks (i.e., jet breaks) of some optical afterglows (Frail et al. 2001; Zeh et al. 2006) and from analysis of BATSE data using some empirical relations (Yonetoku et al. 2005). There are several suggestions of events with very small  $\theta_j$  (e.g., Schady et al. 2007; Racusin et al. 2008), although the value of  $q_1$  is highly uncertain. The spectral parameters  $r_0^2 A_0$ ,  $\gamma v'_0$ ,  $\alpha$ , and  $\beta$  are assumed as follows. The first two parameters are given so that the rest-frame spectral peak energies and isotropic  $\gamma$ -ray energies calculated for a jet viewed with  $\theta_v = 0$  are consistent with those of typical GRBs. Such an on-axis emission has approximately  $E_p = 2\gamma v'_0$  and  $E_{\text{iso}} = 16\pi^2 r_0^2 A_0 \gamma v'_0$ . The parameters  $r_0^2 A_0$  and  $\gamma v'_0$  are given through the empirical relations  $E_{\text{iso}} \theta_j^2 / 2 = 10^{51} \xi_1$  erg and  $E_p = 80 \xi_2 (E_{\text{iso}} / 10^{52} \text{ erg})^{1/2}$  keV (e.g., Frail et al. 2001; Amati

<sup>12</sup> We confirmed that the bursts with  $\theta_v \geq 0.22$  rad in our simulation are not detected by *HETE-2* or *POET* with the parameters we adopt in this paper. We can, therefore, discuss the distribution of several quantities of the detectable bursts and the event rate ratio of bursts for which polarizations can be measured to the detectable bursts without considering the bursts with  $\theta_v \geq 0.22$  rad.

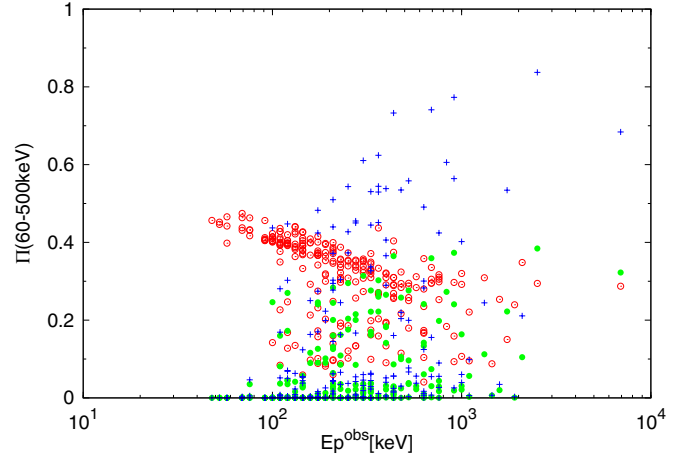


**Figure 6.**  $E_{p,\text{obs}} - \Pi$  diagrams for the simulated events that can be detected by GRAPE in the SO (red open circles), SR (green filled circles), and CD (blue plus signs) models. The adopted parameters are as follows. The fixed parameters are  $\gamma = 100$ ,  $q_1 = 0.5$ ,  $q_2 = -2.0$ ,  $\alpha = -0.2$ ,  $\beta = 1.2$ , and  $T = 20$  s. The distribution of the source redshift  $z$  is assumed to be in proportion to the cosmic star formation rate. The parameters  $r_0^2 A_0$  and  $\gamma v'_0$  are distributed so that the simulated  $E_{p,\text{obs}} - F$  diagram is consistent with the observed data (see Figure 5). See text for the cases of the spectral indices distributed realistically, for  $-0.5 < \alpha < 0.4$  and  $0.9 < \beta < 1.8$ .

(A color version of this figure is available in the online journal.)

et al. 2002). We assume that the coefficients  $\xi_1$  and  $\xi_2$  obey the lognormal distribution (Ioka & Nakamura 2002) with averages of 1 and logarithmic variances of 0.3 and 0.15, respectively. The last two parameters are fixed by  $\alpha = -0.2$  and  $\beta = 1.2$ , which are typical values for GRB prompt emission (Preece et al. 2000; Sakamoto et al. 2005). The distribution of the source redshift,  $z$ , is assumed to be in proportion to the cosmic star-formation rate. We adopt the model SF2 in Porciani & Madau (2001), i.e., the comoving GRB rate density is assumed to be proportional to

$$R(z) = \frac{\exp(3.4z)}{\exp(3.4z) + 22} \frac{\sqrt{\Omega_M(1+z)^3 + \Omega_\Lambda}}{(1+z)^{3/2}}. \quad (19)$$

We take the standard cosmological parameters of  $H_0 = 70$  km s<sup>-1</sup> Mpc<sup>-1</sup>,  $\Omega_M = 0.3$ , and  $\Omega_\Lambda = 0.7$ .

Figure 5 shows the results of  $E_{p,\text{obs}}$  and time-averaged flux,  $F$ . The time-averaged flux is calculated by  $F = I/T$ , where  $T$  is the duration of a burst. We fix  $T = 20$  s, which is a typical value for long GRBs (e.g., Sakamoto et al. 2005). We show only the simulated bursts that have fluxes above the detectable limit of the *HETE-2* satellite. They are consistent with the data obtained by *HETE-2* (Sakamoto et al. 2005). The scatter of the simulated bursts is due to both the scatter of the assumed jet parameters and the viewing angle effect (Yamazaki et al. 2004; Donaghy 2006).<sup>13</sup>

#### 4.2. Properties of Polarization Distribution

We calculated the linear polarization,  $\Pi$ , by using Equations (11), (16), and (17) to obtain the polarization distribution of the simulated bursts that can be detected by GRAPE and LEP. The detection limits of GRAPE and LEP are set to be the MDP contours of 1.0 (see Figure 1).<sup>14</sup> Figures 6 and 7 show the

<sup>13</sup> Yamazaki et al. (2004) showed a deviation from the Amati relation ( $E_p \propto E_{\text{iso}}^{1/2}$ ) for  $E_p < 10$  keV in the uniform jet model, but the  $E_{p,\text{obs}} - F$  diagram we derive is still consistent with the observed data set.

<sup>14</sup> The detection limits of GRAPE and LEP for signal-to-noise ratio  $> 5$  are similar but not identical to the MDP contours of 1.0. Thus, our setting for the detection limits is just for simplicity.

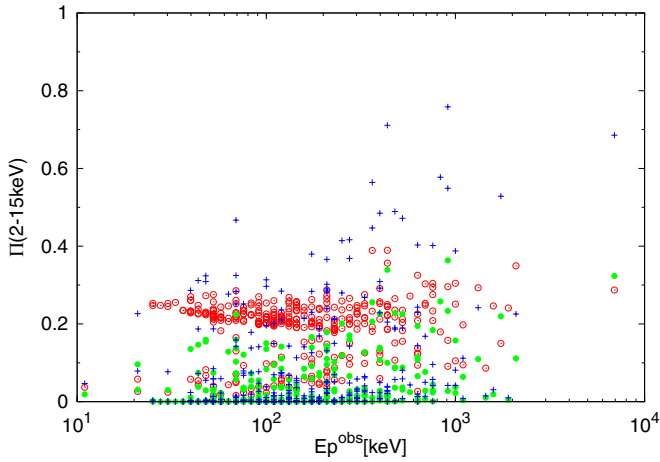


Figure 7. Same as Figure 7, but for LEP.

(A color version of this figure is available in the online journal.)

$E_{p,obs} - \Pi$  diagrams of all the simulated bursts that can be detected by GRAPE and LEP, respectively, in the SO (red open circles), SR (green filled circles), and CD (blue plus signs) models. In the SO model, most of the detectable bursts have  $0.3 < \Pi < 0.5$  in the GRAPE band (60–500 keV), while they have  $0.2 < \Pi < 0.3$  in the LEP band (2–15 keV). In the SR and CD models, most of the detectable bursts have  $\Pi < 0.1$  in both GRAPE and LEP bands. The events with  $\Pi \geq 0.1$  are distributed uniformly with  $\Pi < 0.4$  and  $\Pi < 0.9$  for the SR and CD models, respectively.

This result can be roughly explained by the polarizations calculated as functions of  $y_j$  and  $q = \theta_v/\theta_j$  for  $\gamma v'_0 = 350$  keV and  $z = 1$  (see Figures 2–4) and the distribution of  $\theta_j$  and  $q$  for the detectable bursts in this simulation shown in Figure 8. The detectable events are dominated by the events with  $q < 1$ , since events with  $q < 1$  are much brighter than those with  $q > 1$  because of the relativistic beaming effect. For events with  $q > 1$ , narrower jets are easier to detect since they have intrinsically higher emissivities by our assumption. Most of the detectable events have  $q < 1$  and  $\theta_j > 0.02$  (i.e.,  $y_j > 4$ ). For these events the SO model gives  $0.3 < \Pi < 0.5$  in most cases, while the SR and CD models give  $\Pi < 0.1$ , for the GRAPE band as shown in Figures 2–4. The remaining detectable events mainly have  $q > 1$  and  $\theta_j > 0.005$  (i.e.,  $y_j > 0.25$ ). These events have  $\Pi < 0.6$  in the SO model,  $\Pi < 0.5$  in the SR model, and  $\Pi < 0.9$  in the CD model, for the GRAPE band as shown in Figures 2–4. The results for the LEP band can be explained similarly.

In all the three models, the results show  $\Pi(60\text{--}500 \text{ keV}) > \Pi(2\text{--}15 \text{ keV})$  for almost all the detectable bursts with  $\Pi > 0.1$ . This is due to the fact that typically the contribution of the high-energy photons with spectral index  $\beta$  is larger in the GRAPE band than in the LEP band. The emission with softer spectrum has higher polarization because of the intrinsic property of the synchrotron polarization (Equation (8)) for the SO and SR models and the kinematic effect for the CD model (see Section 3.3), respectively.

In the SO model, the polarization of GRBs with  $q < 1$  is higher for lower  $E_{p,obs}$  for the GRAPE band. This is because the contribution from high-energy photons, with energy spectral index  $\beta$ , is larger. In the SR and CD models, the higher  $\Pi$  GRBs can be obtained for smaller  $\theta_j$ . The maximum  $\Pi$  is obtained for  $\theta_j \simeq 0.002$ .

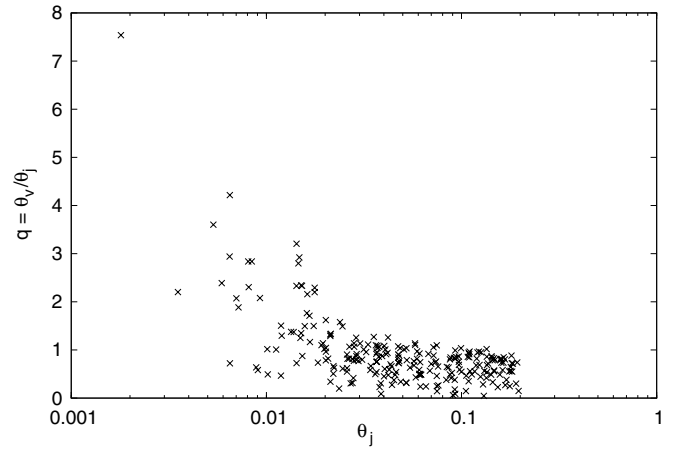


Figure 8. Distribution of  $\theta_j$  and  $q = \theta_v/\theta_j$  of the detectable bursts by GRAPE in the model described by Figure 6.

### 4.3. Cumulative Distribution of Measurable Polarizations

We obtain the distribution of polarization that can be measured, by using the MDP values we derived for  $\alpha = -0.2$ ,  $\beta = 1.2$ , and  $T = 20$  s (see Section 2). We interpret the simulated events with  $\Pi > \text{MDP}$  as “ $\Pi$ -measurable events.” Figure 9 shows the cumulative distribution of  $\Pi$  that can be measured by GRAPE and LEP in the SO, SR, and CD models. We have set the number of detectable events  $N_d = 200$ . Since the polarization in the LEP band is lower than in the GRAPE band for almost all the cases as discussed in Section 4.2, the number of events for which polarization can be measured by LEP is smaller than for GRAPE. In the SO model, the number of  $\Pi$ -measurable bursts is  $N_m > 60$ , and the cumulative distribution of measurable  $\Pi$  varies rapidly at  $0.3 < \Pi < 0.4$  for the GRAPE band. In the SR model,  $N_m < 10$ , and the maximum polarization is  $\Pi_{\max} < 0.4$ . In the CD model,  $N_m < 30$ , and  $\Pi_{\max} < 0.8$ .

To investigate general properties of the cumulative distribution that do not depend on the model parameters, we performed simulations for other values of  $\gamma$ ,  $q_1$ , and  $q_2$ , the Lorentz factor of the jets and the power-law indices of the distribution of the opening angles of the jets, respectively. We refer to the parameters adopted for the above simulation as “typical” parameters. We now consider a range of parameters:  $\gamma \geq 100$ ,  $q_1 \geq 0.5$ , and  $q_2 \geq -3.0$ , which are quite reasonable for GRBs (e.g., Lithwick & Sari 2001; Yonetoku et al. 2005). Within these parameter ranges we obtain the lower (upper) limit of  $N_m/N_d$  for the SO model (the SR/CD models).

Figure 10 shows the results for  $\gamma = 300$  and the same “typical” values for the other parameters. The number  $N_m$  is larger in the SO model and smaller in the SR and CD models than the case of  $\gamma = 100$ . As  $\gamma$  is larger, the beaming effect is stronger and the ratio of the bursts with  $q < 1$  for detectable bursts is larger. Thus, the number of bursts with a high degree of polarization is larger in the SO model and smaller in the SR and CD models. Figure 11 shows the results for  $q_1 = 1.0$  and the same “typical” values for the other parameters. Since the ratio of the number of the bursts with smaller  $y_j$  to that of detectable bursts is smaller,  $N_m$  is slightly smaller than that for the “typical” parameters in the SR and CD models. Figure 12 shows the results for  $q_2 = -3.0$  and the “typical” values for the other parameters. In this case  $N_m$  is slightly larger than that for the “typical” parameters in the SR and CD models.

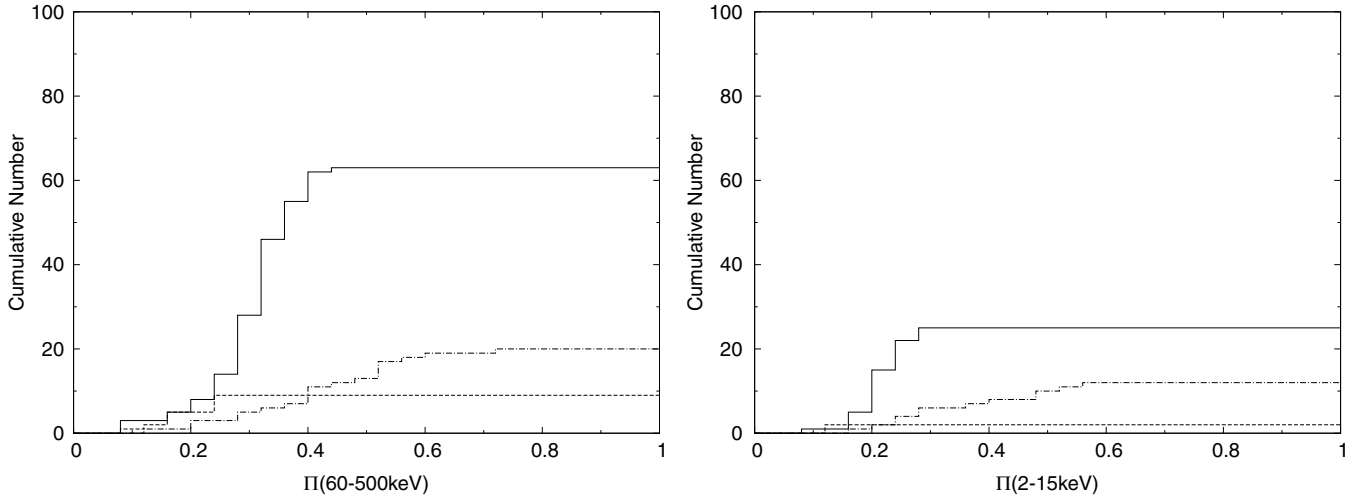


**Figure 9.** The cumulative distribution of  $\Pi$  that can be measured by GRAPE (left) and LEP (right) in the SO (solid), SR (dashed), and CD (dot-dashed) models in which the number of detectable bursts is 200. The adopted parameters are as follows. The fixed parameters are  $\gamma = 100, q_1 = 0.5, q_2 = -2.0, \alpha = -0.2, \beta = 1.2,$  and  $T = 20$  s. The distribution of the source redshift  $z$  is assumed to be in proportion to the cosmic star formation rate. The parameters  $r_0^2 A_0$  and  $\gamma v'_0$  are distributed so that the simulated  $E_{p,obs} - F$  diagram is consistent with the observed data (see Figure 5). See text for the cases of the spectral indices distributed realistically, for  $-0.5 < \alpha < 0.4$  and  $0.9 < \beta < 1.8$ .

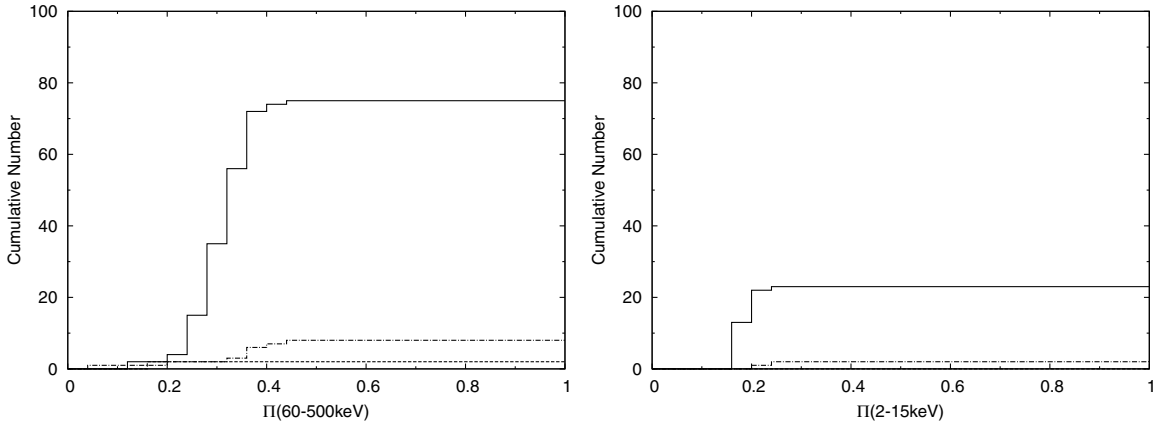


**Figure 10.** Same as Figure 9, but the Lorentz factor of the jets  $\gamma = 300$ .

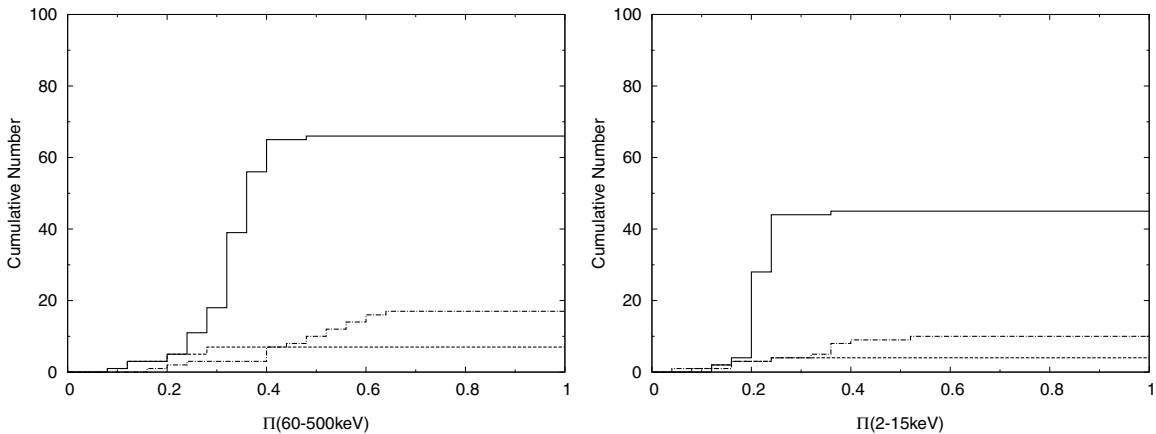


**Figure 11.** Same as Figure 9, but the lower power-law index of the  $\theta_j$  distribution  $q_1 = 1.0$  (see Equation (18)).

The number  $N_m$  in the SO model is similar for Figures 9, 11, and 12 in the GRAPE band. To summarize, for the parameters  $\gamma \geq 100, q_1 \geq 0.5, q_2 \geq -3.0, \alpha = -0.2$  and  $\beta = 1.2,$  we can say that  $N_m/N_d > 30\%$  for GRAPE and the cumulative distribution of measurable  $\Pi$  varies rapidly from  $0.3 < \Pi < 0.4$  in the SO model. For the SR model,  $N_m/N_d < 5\%$  for GRAPE,

with a maximum polarization  $\Pi_{max} < 0.4$ . For the CD model,  $N_m/N_d < 15\%$  for GRAPE, and  $\Pi_{max} < 0.8$ .

Since the dependence of the polarization degree on the spectral indices is relatively large in the SO and SR models, we should take account of the distribution of  $\alpha$  and  $\beta$ . The observed spectral parameters  $\alpha$  and  $\beta$  are distributed roughly

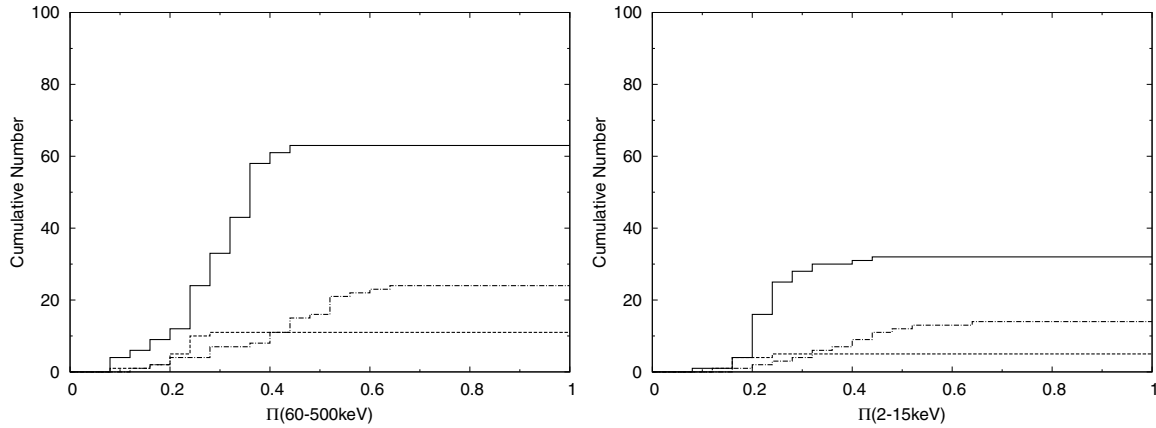


**Figure 12.** Same as Figure 9, but the higher power-law index of the  $\theta_j$  distribution  $q_2 = -3.0$  (see Equation (18)).

as  $-0.5 < \alpha < 0.4$  and  $0.9 < \beta < 1.8$  (Preece et al. 2000; Sakamoto et al. 2005). Within these ranges of  $\alpha$  and  $\beta$ , the polarization degree for  $y_j > 10$ ,  $q < 1$ , and  $50 < E_{p,obs} < 10^3$  keV is  $0.2 < \Pi < 0.7$  in the SO model. Thus, the measurable polarizations are clustered at  $0.2 < \Pi < 0.7$ . The maximum polarization obtained in the SO model for  $y_j \geq 0.01$ ,  $\alpha \leq 0.4$ , and  $\beta \leq 1.8$  is  $\simeq 0.8$  (see Section 3.1). In this case,  $N_m/N_d$  will be larger than 30%. In the CD model, the result will not be significantly different from the case of fixed  $\alpha$  and  $\beta$ . In the SR model, the polarization degree does not exceed those calculated in the CD model, and thus  $N_m/N_d < 15\%$ . The maximum polarization obtained in the SR model for  $y_j \geq 0.01$ ,  $\alpha \leq 0.4$ , and  $\beta \leq 1.8$  is  $\simeq 0.8$  (see Section 3.2).

In conclusion, we can constrain the emission mechanism of GRBs by using the cumulative distribution obtained by GRAPE. If  $N_m/N_d > 30\%$ , the SR and CD models may be ruled out, and in this case if the measured polarizations are clustered at  $0.2 < \Pi < 0.7$ , the SO model will be favored. If  $N_m/N_d < 15\%$ , the SO model may be ruled out, but we cannot distinguish between the SR and CD models with different distributions of  $y_j$ ,  $\alpha$ , and  $\beta$ . If several bursts with  $\Pi > 0.8$  are detected, however, the CD model which includes adequate number of small  $y_j$  bursts will be favored.

## 5. SUMMARY AND DISCUSSION

Recently, there has been an increasing interest in the measurement of X-ray and  $\gamma$ -ray polarization, and the observational techniques can now achieve significant sensitivity in the relevant energy bands. Several polarimetry mission concepts, such as *POET*, are being planned. The *POET* concept has two polarimeters, GRAPE (60–500 keV) and LEP (2–15 keV), both of which have wide FoVs. If launched, missions of this type would provide the first definitive detection of the polarization of GRB prompt emission. This would enable the discussion of the statistical properties of the polarization degree and polarization spectra, which will give us diagnostic information on the emission mechanism of GRBs and the nature of the GRB jets that cannot be obtained from current spectra and light-curve observations. We have performed Monte Carlo simulations of the linear polarization from GRB jets for three major emission models: the synchrotron model with globally ordered magnetic field (SO model), the synchrotron model with small-scale random magnetic field (SR model), and the Compton drag model (CD model). We assumed that the physical quantities for the emission of the jets are uniform on the emitting surface and that the jets

have sharp edges. Our jet angle distribution allows the detections of GRBs with very small opening angles (i.e., smaller than  $1^\circ$ ) as suggested by several *Swift* bursts (Schady et al. 2007; Racusin et al. 2008). We have shown that the *POET* mission or other polarimeters with similar capabilities, i.e., broadband spectral capabilities for the determination of  $E_{p,obs}$  and sensitive broadband polarimetric capabilities to minimize MDP, can constrain the emission models of GRBs. Furthermore, these simulations indicate that an increase in the LEP effective area would be beneficial to compensate for the lower expected polarization at lower energies.

As shown in Figures 2–4, the SR and CD models require off-axis observations of the jets to achieve a high level of polarization, while the SO model does not. In this sense, the SR and CD models are categorized as *geometric* models, and the SO model as an *intrinsic* model (Waxman 2003; Lazzati 2006). The distribution of observed polarizations obtained by our simulations show that the geometric SR/CD models will be ruled out if the number ratio of the  $\Pi$ -measurable bursts to detected bursts is larger than 30%, and in this case, the SO model will be favored if the measurable polarizations are clustered at  $0.2 < \Pi < 0.7$ . If the number ratio is smaller than 15%, the SO model may be ruled out, but we cannot distinguish between the SR and CD models with different distributions of  $y_j = (\gamma\theta_j)^2$ ,  $\alpha$ , and  $\beta$ , where  $\gamma$  and  $\theta_j$  are the bulk Lorentz factor and the opening angle of the GRB jet, respectively, and  $\alpha$  and  $\beta$  are lower and higher indices of the energy spectrum. However, if several bursts with  $\Pi > 0.8$  are detected, the CD model which includes an adequate number of small  $y_j$  bursts will be favored.

If the cumulative distribution of the measurable polarizations favors the SO model, the globally ordered magnetic field would be advected from the central engine. If we understand the strength of the magnetic field in the emitting region from the luminosity and the spectrum of the emission, we can constrain the strength of the field at the central engine. If the geometric SR/CD models are favored from the observations, it will be established, independent of the afterglow observations, that GRB outflows are not spherical but highly collimated. If the CD model is favored by the observations, we may constrain the distribution of the parameter  $y_j = (\gamma\theta_j)^2$  of GRB jets. The CD model needs a dense optical/UV photon field interacting within the relativistic jets (Lazzati et al. 2000; Eichler & Levinson 2003).

We have made some simplifications in our simulations, and there are some caveats. We have assumed that the jets are uniform on the emitting surfaces and have sharp edges. To

compare the simulations and the observations further, more sophisticated modeling is required (e.g., Zhang et al. 2004; Toma et al. 2005).

We have interpreted bursts as a simple combination of pulses, without taking account of the temporal variation of the Lorentz factor  $\gamma$  of the jet. If this is accounted for, each pulse may have different  $y_j = (\gamma\theta_j)^2$  but the same  $q = \theta_v/\theta_j$ . We should then average the polarization with respect to fluence of each pulse having different  $y_j$  (Granot 2003; Nakar et al. 2003). However, in the SO model, the cumulative distribution of measurable  $\Pi$  will not be changed significantly as long as  $y_j > 10$ , because  $\Pi$  is clustered into a small range for  $q < 1$  and  $y_j > 10$ . To average the polarization in the case of  $q > 1$ , the relation between the luminosity and the Lorentz factor for each pulse is required to predict the polarization distribution.

For the SR model we have assumed that the directions of the magnetic field are confined within the shock plane. They may be more isotropic in reality, in which case the polarization degree in the SR model will be reduced.

In the synchrotron model with a combination of the globally ordered magnetic field and the locally random field,  $\mathbf{B} = \mathbf{B}_{\text{ord}} + \mathbf{B}_{\text{rnd}}$ , the linear polarization can be calculated by  $\Pi = (Q_{\text{ord}} + Q_{\text{rnd}})/(I_{\text{ord}} + I_{\text{rnd}}) \approx (\Pi_{\text{ord}} + \eta\Pi_{\text{rnd}})/(1 + \eta)$ , where  $\{I, Q\}_{\text{ord}}$  and  $\{I, Q\}_{\text{rnd}}$  are the Stokes parameters from the ordered and random fields, respectively. Here,  $\Pi_{\text{ord}}$  and  $\Pi_{\text{rnd}}$  are described by Equations (11) and (16), and  $\eta \equiv (B_{\text{rnd}}/B_{\text{ord}})^{\alpha+1}$ . This model will reduce the number ratio of  $\Pi$ -measurable bursts to detected bursts to less than 30% and the clustering of measurable polarizations will be at  $\Pi < 0.7$ .

This work is supported in part by the grant-in-aid from the Ministry of Education, Culture, Sports, Science and Technology (MEXT) of Japan, No. 19047004 (R.Y., K.I., and T.N.), No. 18740153 (R.Y.), No. 18740147 (K.I.), No. 19540283 (T.N.), and in part by the Grant-in-Aid for the global COE program *The Next Generation of Physics, Spun from Universality and Emergence* from the MEXT of Japan. B.Z. acknowledges NASA NNG05GB67G and NNX08AE57A (Nevada NASA EPSCoR program) and K.T. acknowledges NASA NNX08AL40G for partial supports.

## APPENDIX

### SOME NOTES ON SYNCHROTRON POLARIZATION

#### A.1. The SO Model: Synchrotron with Ordered Field

We consider the synchrotron radiation from the shell moving radially outward with a bulk Lorentz factor  $\gamma \gg 1$ , and the magnetic field in the shell is globally ordered within the plane parallel to the shock plane. If the matter of the shell expands with a constant speed, the strength of magnetic field with radial direction scales as  $R^{-2}$  while that with transverse direction scales as  $R^{-1}$ . Thus, the field advected with the shell is likely to have the direction parallel to the shock plane.

We set the line of sight (i.e., the direction from the central engine to the earth) in the lab frame to be  $z$  axis, and the direction of the magnetic field on a given point of the shell, projected onto the plane perpendicular to  $z$  axis, to be  $\bar{x}$  axis. The given point can be described by spherical coordinates  $(\theta, \varphi)$ . Then the components of the velocity vector of the given point and the unit wavevector can be described by the right-handed coordinate system  $\bar{x}\bar{y}\bar{z}$  as  $\beta = (\beta \sin \theta \cos \varphi, \beta \sin \theta \sin \varphi, \beta \cos \theta)$  and  $\hat{\mathbf{k}} = (0, 0, 1)$ , respectively. The unit wavevector in the comoving

frame is

$$\hat{\mathbf{k}}' = \frac{1}{\gamma(1 - \beta \cdot \hat{\mathbf{k}})} \left[ \hat{\mathbf{k}} + \beta \left( \frac{\gamma^2}{\gamma + 1} \beta \cdot \hat{\mathbf{k}} - \gamma \right) \right]. \quad (\text{A1})$$

Since the direction of the magnetic field in the comoving frame is perpendicular to the velocity vector of the fluid,  $\hat{\mathbf{B}}' = (\cos \theta / \sqrt{\cos^2 \theta + \sin^2 \theta \cos^2 \varphi}, 0, -\sin \theta \cos \varphi / \sqrt{\cos^2 \theta + \sin^2 \theta \cos^2 \varphi})$ . Then we may calculate  $\cos \theta'_B = \hat{\mathbf{B}}' \cdot \hat{\mathbf{k}}'$ , and we obtain

$$\sin \theta'_B \approx \left( \frac{1 - \gamma^2 \theta^2}{1 + \gamma^2 \theta^2} \right)^2 \cos^2 \varphi + \sin^2 \varphi \quad (\text{A2})$$

in the limit  $\gamma \gg 1$ .

The direction of the polarization vector of the synchrotron radiation is calculated by  $\mathbf{e}' \parallel \hat{\mathbf{B}}' \times \hat{\mathbf{k}}'$ . Then we obtain the direction of the polarization vector in the lab frame by

$$\mathbf{e} = \gamma(1 + \beta \cdot \hat{\mathbf{k}}')\mathbf{e}' - (\beta \cdot \mathbf{e}') \left( \frac{\gamma^2}{\gamma + 1} \beta + \gamma \hat{\mathbf{k}}' \right). \quad (\text{A3})$$

The results are  $e_z = 0$  and

$$\tan \chi_B \equiv \frac{e_y}{e_x} = \tan \varphi - \frac{\beta - \cos \theta}{\beta \sin^2 \theta} \frac{1}{\sin \varphi \cos \varphi}. \quad (\text{A4})$$

The angle  $\chi_B$  is the polarization position angle measured from the axis  $\bar{x}$  (i.e., the direction of the local magnetic field). The above equation can be rewritten as  $\chi_B \approx \varphi + \arctan[(1 - \gamma^2 \theta^2) \cot \varphi / (1 + \gamma^2 \theta^2)]$ . This result is consistent with that of Granot (2003).

Based on the above results, we consider the case that the magnetic field is axisymmetric around the jet and has a toroidal configuration. We set the direction from the line of sight to the jet axis to be  $x$  axis. Below we will rewrite the above results by using the azimuthal angle  $\phi$  measured from  $x$ -axis. In the coordinate system of  $xyz$ , the jet axis and the coordinates of a given point on the shell are described as  $\mathbf{J} = (\sin \theta_v, 0, \cos \theta_v)$ , and  $\mathbf{R} = (\sin \theta \cos \phi, \sin \theta \sin \phi, \cos \theta)$ , respectively. The magnetic field at the given point is given by  $\hat{\mathbf{B}}' = \mathbf{R} \times \mathbf{J} / |\mathbf{R} \times \mathbf{J}|$ . Let the unit vectors of the directions of  $\mathbf{R}$  and  $\hat{\mathbf{B}}'$  projected onto  $xy$  plane be  $\hat{\mathbf{r}}$  and  $\hat{\mathbf{b}}$ , and  $\cos \varphi = \hat{\mathbf{b}} \cdot \hat{\mathbf{r}}$ . Then we obtain

$$\cos^2 \varphi \approx \frac{\sin^2 \phi}{1 + a^2 - 2a \cos \phi}, \quad (\text{A5})$$

where  $a \equiv \theta/\theta_v$ . Equation (9) is given by inserting Equation (5) into Equation (2). If we measure the position angle from the  $x$  axis, we obtain Equation (10), i.e.,  $\chi = \chi_B - \varphi + \phi$ . These results are consistent with those of Granot & Taylor (2005).

#### A.2. The SR Model: Synchrotron with Random Field

Here, we consider that the directions of the magnetic fields are confined within the plane parallel to the shock plane and that they are completely random. This field configuration is possible if the field is generated by the shock. In the comoving frame of the shell, we set the direction of  $\hat{\mathbf{k}}'$  to be axis 3, and set a right-handed coordinate system 123. Let the polar and azimuthal angles of  $\hat{\mathbf{B}}'$  be  $\theta'_B$  and  $\phi'_B$ , respectively. In this coordinate system, the Stokes parameters of synchrotron emissivity are given by

$$j'_v{}^Q = -j'_v{}^I \Pi_0 \cos(2\phi'_B), \quad j'_v{}^U = -j'_v{}^I \Pi_0 \sin(2\phi'_B). \quad (\text{A6})$$

Next, we set another right-handed coordinate system  $xyz$  of which  $z$ -axis is along the velocity vector of the fluid and  $x$ - $z$  plane includes  $\mathbf{k}'$ . Then the angle between  $\mathbf{k}'$  and  $z$ -axis is  $\theta'$ . Here the magnetic field  $\mathbf{B}'$  is confined within  $x$ - $y$  plane. Let the azimuthal angle of  $\mathbf{B}'$  be  $\eta'$ , and we obtain the relations between the components of  $\mathbf{B}'$  in the systems 123 and  $xyz$ .

$$\begin{aligned} \sin \theta'_B \sin \phi'_B &= \cos \theta' \cos \eta', \\ \sin \theta'_B \cos \phi'_B &= \sin \eta', \\ \cos \theta'_B &= \sin \theta' \cos \eta'. \end{aligned} \quad (\text{A7})$$

Then we obtain

$$\begin{aligned} \sin \theta'_B &= \left[ 1 - \frac{4\gamma^2\theta^2}{(1+\gamma^2\theta^2)^2} \cos^2 \eta' \right]^{1/2}, \\ \cos(2\phi'_B) &= \frac{1}{\sin^2 \theta'_B} \left[ \sin^2 \eta' - \left( \frac{1-\gamma^2\theta^2}{1+\gamma^2\theta^2} \right)^2 \cos^2 \eta' \right]. \end{aligned} \quad (\text{A8})$$

To obtain the polarization degree of synchrotron radiation from the random field, we average the Stokes parameters with respect to  $\eta'$ . This leads to  $\langle j'_{\nu^U} \rangle = 0$ . Then we can calculate the polarization degree by  $\Pi_0 = \langle j'_{\nu^Q} \rangle / \langle j'_{\nu^I} \rangle = \Pi_0^{\text{syn}} \langle (\sin \theta'_B)^{\alpha+1} \cos(2\phi'_B) \rangle / \langle (\sin \theta'_B)^{\alpha+1} \rangle$ , and the polarization vector is along axis 1, i.e., the direction perpendicular to  $\mathbf{k}'$  and within the plane including  $\mathbf{k}'$  and  $\beta$ .

## REFERENCES

- Amati, L. 2002, *A&A*, **390**, 81  
Band, D. L., et al. 1993, *ApJ*, **413**, 281  
Begelman, M. C., & Sikora, M. 1987, *ApJ*, **322**, 650  
Black, J. K., et al. 2007, *NIMA*, **581**, 755  
Bloser, P. F., et al. 2006, *ChJAS*, **6**, 393  
Bloser, P. F., et al. 2009, *NIMA*, **600**, 424  
Boggs, S. E., et al. 2006, NASA Vision Mission Concept Study Report (arXiv:astro-ph/0608532)  
Coburn, W., & Boggs, S. E. 2003, *Nature*, **423**, 415  
Costa, E., et al. 2007, *Proc. SPIE*, **6686**, 30  
Covino, S., Ghisellini, G., Lazzati, D., & Malesani, D. 2004, in ASP Conf. Ser. 312, Third Rome Workshop on Gamma-Ray Bursts in the Afterglow Era, ed. M. Feroci et al. (San Francisco, CA: ASP), 169  
Dai, X., & Zhang, B. 2005, *ApJ*, **621**, 875  
Donaghy, T. Q. 2006, *ApJ*, **645**, 436  
Eichler, D., & Levinson, A. 2003, *ApJ*, **596**, L147  
Fendt, C., & Ouyed, R. 2004, *ApJ*, **608**, 378  
Frail, D. A., et al. 2001, *ApJ*, **562**, L55  
Ghisellini, G., & Lazzati, D. 1999, *MNRAS*, **309**, L7  
Granot, J. 2003, *ApJ*, **596**, L17  
Granot, J., Piran, T., & Sari, R. 1999, *ApJ*, **513**, 679  
Granot, J., & Taylor, G. B. 2005, *ApJ*, **625**, 263  
Greiner, J., et al. 2008, in AIP Conf. Proc. 1000, Gamma-Ray Burst Investigation via Polarimetry and Spectroscopy, ed. M. Galassi, D. Palmer, & E. Fenimore (Melville, NY: AIP), 620  
Gruzinov, A., & Waxman, E. 1999, *ApJ*, **511**, 852  
Hill, J. E., et al. 2008, in Proc. of 2008 Nanjing GRB Conference, AiPC, 1065, 331  
Hjorth, J. 2003, *Nature*, **423**, 847  
Ioka, K., & Nakamura, T. 2001, *ApJ*, **554**, L163  
Ioka, K., & Nakamura, T. 2002, *ApJ*, **570**, L21  
Ioka, K., et al. 2007, *ApJ*, **670**, L77  
Jahoda, K., et al. 2007, arXiv:astro-ph/0701090  
Jason, L., et al. 2005, *Proc. SPIE*, **5898**, 413  
Kalemci, E., et al. 2007, *ApJS*, **169**, 75  
Lazzati, D. 2006, *New J. Phys.*, **8**, 131  
Lazzati, D., Ghisellini, G., Celotti, A., & Rees, M. J. 2000, *ApJ*, **529**, L17  
Lazzati, D., Rossi, E., Ghisellini, G., & Rees, M. J. 2004, *MNRAS*, **347**, L1  
Levinson, A., & Eichler, D. 2004, *ApJ*, **613**, 1079  
Lithwick, Y., & Sari, R. 2001, *ApJ*, **555**, 540  
Lytikov, M., Pariev, V. I., & Blandford, R. D. 2003, *ApJ*, **597**, 998  
Matsumiya, M., & Ioka, K. 2003, *ApJ*, **595**, L25  
McGlynn, S., et al. 2007, *A&A*, **466**, 895  
Medvedev, M. V., & Loeb, A. 1999, *ApJ*, **526**, 697  
Mészáros, P. 2006, *Rep. Prog. Phys.*, **69**, 2259  
Mizuno, T., et al. 2005, *Nucl. Instrum. Methods. Phys. Res. Sec. A*, **540**, 158  
Mundell, C. G., et al. 2007, *Science*, **315**, 1822  
Nakar, E., Piran, T., & Waxman, E. 2003, *JCAP*, **10**, 5  
Panaitescu, A., & Mészáros, P. 2000, *ApJ*, **544**, L17  
Piran, T. 2005, *Rev. Mod. Phys.*, **76**, 1143  
Porciani, C., & Madau, P. 2001, *ApJ*, **548**, 522  
Preece, R. D., et al. 2000, *ApJS*, **126**, 19  
Produit, N., et al. 2005, *Nucl. Instrum. Methods. Phys. Res. Sec. A*, **550**, 616  
Racusin, J. L., et al. 2008, *Nature*, **455**, 183  
Rees, M. J., & Mészáros, P. 1994, *ApJ*, **430**, L93  
Rutledge, R. E., & Fox, D. B. 2004, *MNRAS*, **350**, 1288  
Rybicki, G. B., & Lightman, A. P. 1979, *Radiative Processes in Astrophysics* (New York: Wiley Interscience)  
Ryde, F., et al. 2006, *ApJ*, **652**, 1400  
Sagiv, A., Waxman, E., & Loeb, A. 2004, *ApJ*, **615**, 366  
Sakamoto, T., et al. 2005, *ApJ*, **629**, 311  
Sari, R. 1999, *ApJ*, **524**, L43  
Schady, P., et al. 2007, *MNRAS*, **380**, 1041  
Shaviv, N. J., & Dar, A. 1995, *ApJ*, **447**, 863  
Spruit, H. C., Daigne, F., & Drenkhahn, G. 2001, *A&A*, **369**, 694  
Stanek, K. Z., et al. 2003, *ApJ*, **591**, L17  
Taylor, G. B., Frail, D. A., Berger, E., & Kulkarni, S. R. 2004, *ApJ*, **609**, L1  
Taylor, G. B., Momjian, E., Philstrom, Y., Ghosh, T., & Salter, C. 2005, *ApJ*, **622**, 986  
Thompson, C., Mészáros, P., & Rees, M. J. 2007, *ApJ*, **666**, 1012  
Toma, K., Ioka, K., & Nakamura, T. 2008, *ApJ*, **673**, L123  
Toma, K., Yamazaki, R., & Nakamura, T. 2005, *ApJ*, **635**, 481  
Waxman, E. 2003, *Nature*, **423**, 388  
Wigger, C., et al. 2004, *ApJ*, **613**, 1088  
Willis, D. R., et al. 2005, *A&A*, **439**, 245  
Woods, E., & Loeb, A. 1999, *ApJ*, **523**, 187  
Yamazaki, R., Ioka, K., & Nakamura, T. 2004, *ApJ*, **606**, L33  
Yonetoku, D., Yamazaki, R., Nakamura, T., & Murakami, T. 2005, *MNRAS*, **362**, 1114  
Zeh, A., Klose, S., & Kann, D. A. 2006, *ApJ*, **637**, 889  
Zhang, B. 2007, *Chin. J. A&A*, **7**, 1  
Zhang, B., Dai, X., Lloyd-Ronning, N. M., & Mészáros, P. 2004, *ApJ*, **601**, L119  
Zhang, B., & Mészáros, P. 2002, *ApJ*, **581**, 1236